Measurement of the orbital angular momentum density of Bessel beams by projection into a Laguerre–Gaussian basis

Christian Schulze,[1,*] Angela Dudley,[2] Robert Brüning,[1]
Michael Duparré,[1] and Andrew Forbes[2]

[1]Institute of Applied Optics, Friedrich Schiller University, Fröbelstieg 1, 07743 Jena, Germany

[2]Council for Scientific and Industrial Research, National Laser Centre, P.O. Box 395, 0001 Pretoria, South Africa

*Corresponding author: christian.schulze@uni-jena.de

Received 27 June 2014; accepted 30 July 2014;
posted 5 August 2014 (Doc. ID 214921); published 4 September 2014

We present the measurement of the orbital angular momentum (OAM) density of Bessel beams and superpositions thereof by projection into a Laguerre–Gaussian basis. This projection is performed by an all-optical inner product measurement performed by correlation filters, from which the optical field can be retrieved in amplitude and phase. The derived OAM densities are compared to those obtained from previously stated azimuthal decomposition yielding consistent results. © 2014 Optical Society of America

OCIS codes: (030.4070) Modes; (080.4865) Optical vortices; (260.6042) Singular optics; (070.6120) Spatial light modulators.

http://dx.doi.org/10.1364/AO.53.005924

1. Introduction

Laser beams carrying orbital angular momentum (OAM) have attracted a lot of interest in recent years owing to their unique properties [1–4], exhibiting a helical phase structure. By transferring their momentum they are able to spin microscopic particles and have hence received attention in the field of optical trapping and particle manipulation [5–9]. In addition, their singular properties have opened new opportunities in nonlinear optics and quantum optics, enabling the entanglement of single photons in a multistate OAM basis [10], and are of great interest for future mode-multiplexed communication strategies using OAM states in free space [11,12], or optical fibers [13], which are reaching the terabit scale currently.

Whereas all of the OAM carrying beams have a helical phase in common, the amplitude distribution can vary. Traditionally, the OAM properties of Laguerre–Gaussian modes were studied intensively [14], but also others, e.g., fiber beams [15] and Bessel beams, were considered [16]. The latter exhibit interesting possibilities, such as their approximate nondiffractive nature and the ability to reconstruct after obstacles [17], which was demonstrated recently at the single photon level [18], making them particularly useful in micromanipulation of particles [19].

The fast development of science focusing on beams carrying OAM was sped up by the ease of generating them using spiral phase plates [20], or fork gratings (holograms), transforming a simple Gaussian beam into a beam with a helical phase structure of tunable OAM [4], which was currently demonstrated at the kHz level [21], and at exotic wavelengths by high harmonic generation or with electron beams [22,23].

1559-128X/14/265924-10$15.00/0

Alternative generation techniques are the transformation from Hermite–Gaussian modes with cylindrical lenses [24], or by inducing microbends in an optical fiber [15]. In addition to those passive methods, the active generation of OAM beams was demonstrated in laser resonators [25,26] and fiber amplifiers [27].

Besides the beam generation, methods for reliable detection and characterization of OAM states are equally required. Different techniques are known; e.g., the fork hologram can be used to reverse the creation process by projecting the OAM beam into a Gaussian mode [28] by using computer-generated holograms [29], which was advanced recently by coupling the OAM beam to a plasmonic wave [30]. A simple qualitative OAM identification is given by the diffraction at a triangular aperture [31]. Other methods include the rotational frequency shift [32,33], dove prism interferometers [34,35], a circular array of coherent receivers [36], application of a nonlinear interferometer [37], and sorters transforming the OAM to transverse momentum with specific refractive elements [38–41] that provide robust and efficient sorting of OAM states in multimode fields even at the single photon level [42]. For micromanipulation of particles, however, not only the detection of single OAM states is of interest, but also the distribution of the OAM, the OAM density. To measure this quantity two methods have been suggested so far, which we refer to as azimuthal [16,43] and modal decomposition [44].

In this work we use the modal decomposition technique to infer the OAM density distribution of Bessel beams and superpositions by projection into a Laguerre–Gaussian basis. By this procedure, the OAM density can be reconstructed with high fidelity with a small number of modes. Since Laguerre–Gaussian modes depict a well-known basis, this procedure depicts an easy to implement method to discover OAM properties of arbitrary beam compositions and is hence considered to benefit micromanipulation studies.

2. Modal Decomposition

A coherent optical field can be described as a weighted superposition of mode fields, provided they form a complete set and are orthogonal to each other:

$$\langle \psi_n, \psi_m \rangle = \iint_{\infty} \psi_n^* \psi_m \mathrm{d}r\mathrm{d}\phi = \delta_{nm}. \tag{1}$$

In free space such mode fields are in a paraxial approximation given by the well-known Laguerre–Gaussian (LG) or Hermite–Gaussian modes, but other solutions, such as Mathieu or Ince–Gaussian beams, are also feasible [45,46]. The complexity of the investigated optical field, but also the kind and scale of the chosen basis, will define how many mode fields are necessary to form the entire field. Consider, e.g., a Bessel beam, which we define as a beam with a Bessel-like amplitude function J_n of order n and azimuthal phase dependence $\exp(in\phi)$, including linear combinations thereof,

$$U(r,\phi) = \sum_n \beta_n J_n(qr)\, \exp(in\phi), \tag{2}$$

where β is a weighting factor and $q = 2.405/w_b$ defines the size of the Bessel beam by the intrinsic radius, w_b, which represents the first zero of $J_0(qr)$.

Despite the fact that Bessel functions fulfill a specific orthogonality relation that is used in Fourier–Bessel series; for example [47], the above beams, $J_n(r)\exp(\mathrm{in}\phi)$ are not orthogonal in the sense of Eq. (1). However, Bessel beams can be described in terms of modes by using, e.g., the LG basis set,

$$U(r,\phi) = \sum_{p,l} c_{p,l} u_{p,l}(r,\phi;w), \tag{3}$$

where $u_{p,l}$ is the LG mode of intrinsic scale, w, and with index, p (radial order), and l (azimuthal order), and $c_{p,l} = \varrho_{p,l}\exp(i\varphi_{p,l})$ is the corresponding coefficient including the amplitude, $\varrho_{p,l}$, and relative phase, $\varphi_{p,l}$, of a mode, which is the phase difference to an arbitrarily chosen reference field. The LG modes satisfy the orthogonality given in Eq. (1), and are, thus, suitable for an optical correlation analysis, particularly because they obey the same phase dependence as the considered Bessel beams.

3. Choice of Basis Set and Scale

For proper reconstruction of the field and, consequently, of the OAM density (see below), a reasonable number of modes for decomposition is necessary. Since LG modes depict an infinite mode set, the proper choice of a limited number of modes might depict a challenging task. If no prior knowledge about, e.g., the azimuthal dependence of the beam is available, an iterative decomposition in an increasing number of modes constitutes a reasonable approach. As a measure for achieved precision, and as a termination criterion, the similarity between the reconstructed beam intensity and a directly measured intensity, e.g., in terms of a 2D cross correlation coefficient, C, can be used [48]. As soon as there is a strong correlation between both intensity patterns (e.g., $C > 95\%$), the chosen number of modes is sufficient to describe the beam and the iterative decomposition can be stopped.

From Eq. (2) it is clear that the so-defined Bessel beams obey the same azimuthal dependence as LG modes. Accordingly, when decomposing a Bessel beam with azimuthal index, l, only LG modes with the same index, l, will be necessary for reconstruction, while the radial index, p, will cover a range of values to reconstruct the ring structure. This reduces the number of modes that need to be considered significantly. The correct l values contained in the Bessel beam can be estimated by correlating the beam with helical phase patterns, $\exp(il\phi)$, and scanning through different azimuthal indices, l,

of the LG modes. Generally, a spectrum of p modes will then be necessary to describe the Bessel beam for each value of l, which can be found iteratively as described above. The width of the p spectrum depends on the scale parameter, w, of the LG modes and on the extent of the Bessel beam that is considered for the OAM measurement. Whereas, mathematically, both Bessel and Gaussian beams are infinitely extended, the Bessel beam converges much slower toward zero ($\propto 1/r$). Although, experimentally generated Bessel beams always exhibit a Gaussian envelope (Bessel–Gaussian beams), this envelope is typically much larger than the extent of the LG modes that are used for decomposition. Accordingly, the LG modes appear finite compared to the Bessel beam, such that an increasing Bessel field requires a growing number of higher-order radial LG modes for reconstruction.

When a suitable basis for modal decomposition is found (e.g., the LG basis), the most crucial parameter left is the spatial scale of the mode set, which is the waist radius of the embedded fundamental Gaussian beam [49,50], i.e., the intrinsic LG radius, w [cf. Eq. (3)]. Mathematically, the decomposition into modes of any intrinsic scale depicts a valid description of a laser beam; however, it was shown that the scale parameter strongly influences the signal-to-noise ratio and measurement time and hence the susceptibility to temporal instabilities and noise [49]. As a solution the scale parameter can be obtained from measuring the beam propagation ratio, M^2, and the beam diameter as outlined in [49], ensuring an optimal modal decomposition with a minimum number of radial modes.

As an example, we consider the decomposition of a single Bessel beam, $J_1(qr)\exp(i\phi)$ into LG modes of varying scale. Figure 1 depicts the number of modes, N, necessary to reconstruct the beam as a function of the intrinsic radius, w, (scale) of the LG mode set. N was defined by the number of the N strongest modes necessary to sum 95% of the total power (sorted by modal power). As can be seen from Fig. 1, there is a clear minimum of the mode number at around 0.4 mm. A similar value is found based on the beam propagation ratio, M^2 [49], although its precise measurement is difficult for a Bessel beam due to its large spatial extension. Regarding Fig. 1, an intrinsic scale of the LG modes from 0.3 to 0.6 mm depicts a reasonable choice to enable a quick and accurate modal decomposition and reconstruction of the OAM density requiring less than ten LG modes.

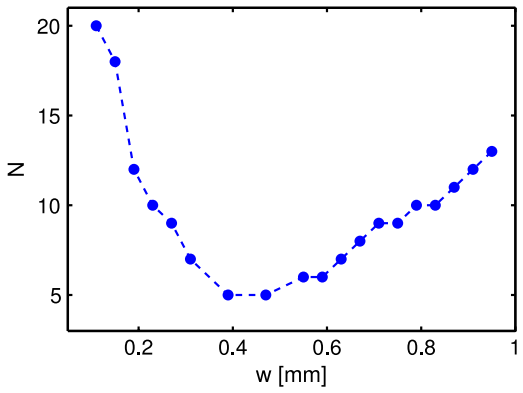

Fig. 1. Simulated number of LG modes $u_{p,l}$ necessary to reconstruct a Bessel beam $J_1\exp(i\phi)$, with indices p ranging from 0 to 30 and $l = 1$, as a function of their intrinsic scale w. The reconstruction area is 1.6 mm × 1.6 mm.

4. Correlation Analysis

The optical correlation analysis intends to measure the complex-valued coefficients, $c_{p,l} = \varrho_{p,l}\exp(i\varphi_{p,l})$, for known (calculated prior to an experiment) mode fields, $u_{p,l}$ [cf. Eq. (3)], and can be performed all-optically using specific diffractive optical elements known as correlation or matched filters [51,52]. The transmission functions T of such elements must be a specific pattern to enable the determination of the amplitude $\varrho_{p,l}$ and relative phase $\varphi_{p,l}$ of each mode, whereas the latter is measured with respect to a certain reference field, e.g., another mode. To extract the amplitude weighting of a mode $u_{p,l}$, the complex conjugate of it, $u^*_{p,l}$, is implemented in the correlation filter. Then the on-axis intensity in the far field is $I_{p,l} = \varrho^2_{p,l}$ [53].

The correlation filter principle is depicted schematically in Fig. 2. An incident distorted wave passes the correlation filter and is focused by a lens ($2f$ arrangement) onto a camera. If the filter's transmission function is matched to the incident wave, i.e., $T = u^*_{p,l}$, the filter will convert the incident wave into a plane wave, which is then focused to a bright on-axis spot at the camera position by cancellation of the phase distortion. If the filter is not matched to the incident wave, no phase cancellation will be achieved and the on-axis intensity will be reduced or even vanish.

This idea of a matched filter can equally be used to measure the mutual phase differences of the modes from writing a transmission function, which is a superposition of the mode field and a reference field [53], by complete analogy to the amplitude measurement described above.

5. Measurement of OAM

Once the coefficients of the modes $c_{p,l}$ have been measured in amplitude and phase, the optical field can be

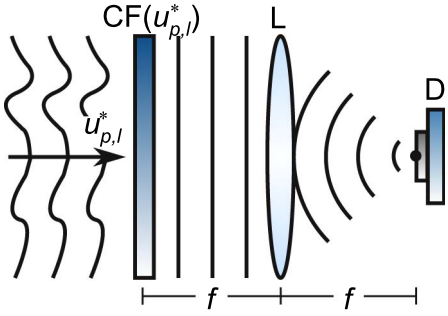

Fig. 2. Illustration of the correlation (matched) filter principle. $u^*_{p,l}$, incident (distorted) wave; CF($u^*_{p,l}$), correlation filter matched to the incident wave; L, lens of focal length f; and D, detector (camera).

reconstructed according to Eq. (3). As a result, the OAM density and the total OAM can be determined from the optical field U. Using the Poynting vector distribution $\mathbf{P}(r,\phi)$,

$$\mathbf{P}(r,\phi) = \frac{\epsilon_0\omega}{4}[i(U\nabla U^* - U^*\nabla U) + 2k|U|^2\mathbf{e}_z], \quad (4)$$

the OAM density $\mathbf{j}$ is inferred by

$$\mathbf{j} = \mathbf{r} \times \frac{\mathbf{P}}{c^2}, \quad (5)$$

where $\mathbf{r} = (r,\phi,z)$, ϵ_0 is the permittivity of vacuum, $\omega = 2\pi c/\lambda$ with wavelength λ and c the speed of light, $k = 2\pi/\lambda$ is the wave number, and $\mathbf{e}_z$ is the unit vector in the z direction. The total OAM then results from the integration in the transverse plane

$$\mathbf{J} = \iint \mathbf{j}(r,\phi)\mathrm{d}r\mathrm{d}\phi. \quad (6)$$

Mostly, the z component of the OAM density, $j_z = rP_\phi/c^2$, is of interest. Referring to the decomposition into LG modes, $u_{p,l} = |u_{p,l}|\exp(il\phi)$ [cf. Eq. (3)], the OAM density j_z can also be inferred from the coefficients $c_{p,l}$ directly by exploiting the dependence on the helical phase,

$$j_z = \frac{\epsilon_0\omega}{2c^2}\sum_{p,p',l,l'} \varrho_{p,l}\varrho_{p',l'}|u_{p,l}u_{p',l'}|l \cdot \cos[(l-l')\phi + \varphi_{p,l} - \varphi_{p',l'}], \quad (7)$$

where p',l' span the same range as p,l. This way, the general approach of reconstructing the Poynting vector distribution [Eq. (4)] can be avoided by direct calculation of the OAM density from the measured modal powers $\varrho^2_{p,l}$ and phases $\varphi_{p,l}$, enabling a faster reconstruction. In the case where the beam consists of modes of the same azimuthal index l (but potentially different radial indices p), the OAM density simplifies to

$$j_z = \frac{\epsilon_0\omega}{2c^2}l\sum_{p,p'}\varrho_{p,l}\varrho_{p',l}|u_{p,l}u_{p',l}|\cos[\varphi_{p,l} - \varphi_{p',l}] = \frac{\epsilon_0\omega}{2c^2}l\left|\sum_p c_{p,l}u_{p,l}\right|^2, \quad (8)$$

which means that the OAM density is directly proportional to the intensity of the beam, whereas the overall sign is determined by the value of l. In the case of a single mode finally, the OAM density becomes $j_z \propto l\rho^2_{p,l}|u_{p,l}|^2$.

6. Experimental Setup

The setup as shown in Fig. 3 was used first to generate the Bessel beams, and second to measure the OAM density by modal decomposition into LG modes. A helium neon laser at 633 nm wavelength (≈10 mW) was expanded using a magnifying telescope to approximate a plane wave, which then illuminated a spatial light modulator (SLM). In the experiments, we used a pixelated reflective SLM based on liquid crystals on silicon (Pluto, Holoeye, 1920 pixels ×1080 pixels, 8 μm pixel pitch). The respective Bessel beams were then generated using a coding technique for computer-generated phase holograms [54]. Accordingly, the near field, U, of the beam of interest was encoded by a phase-only function, $h = \exp[i\Psi(r,\phi)]$, where Ψ is determined from the ansatz, $\Psi(r,\phi) = f(|U|)\sin[\arg(U)]$, and $J_1[f(|U|)] = 0.58|U|$. Using this technique for complex amplitude modulation, the desired beam was generated in the first diffraction order of the SLM. To separate the generated beam from undiffracted light (zeroth order), a grating was superimposed such that $\Psi = \Psi[\arg(U) + 2\pi(f_x x + f_y y); |U|]$. The first diffraction order was selected by an aperture in the far field plane of the SLM. To determine the OAM density, the beams were incident on a second SLM (SLM_2, correlation filter), which performed the modal decomposition in combination with a $2f$ setup and a camera (CCD_1), applying the principle as introduced in Section 4. The complex-valued transmission functions necessary to measure the amplitudes and relative phases of all LG modes were encoded the same way as the Bessel beams for their generation, i.e., the main principles of the correlation filter method could be used for both beam generation and analysis. At the same time, the generated beam was $4f$, imaged from SLM_1 to a second camera CCD_2 to directly record the near field intensity. This way, the reconstructed intensity could be compared to the directly measured one using a 2D cross correlation coefficient [48], indicating the success of the modal decomposition experiment.

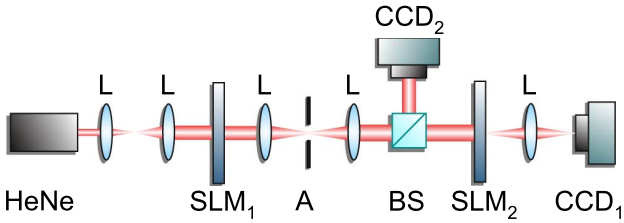

Fig. 3. Scheme of the experimental setup. HeNe, helium neon laser; L, lens; $\mathrm{SLM}_{1,2}$, spatial light modulators (reflective, shown in transmission to ease presentation); A, aperture; BS, beam splitter; $\mathrm{CCD}_{1,2}$, cameras.

7. OAM Density of Bessel Beams

To demonstrate the procedure of inferring the OAM density, a simple LG beam $u_{0,1}$ was generated with SLM_1 by displaying a transmission function, $T = u^*_{0,1}$ (cf. Sections 5 and 6). A second SLM (SLM_2) and a camera following a $2f$ setup were used to modally decompose the beam and to measure the OAM density, pretending not to know which beam was generated, i.e., decomposing into a large number of modes. Figure 4 depicts the measurement results for characterizing the LG beam $u_{0,1}$ by decomposition

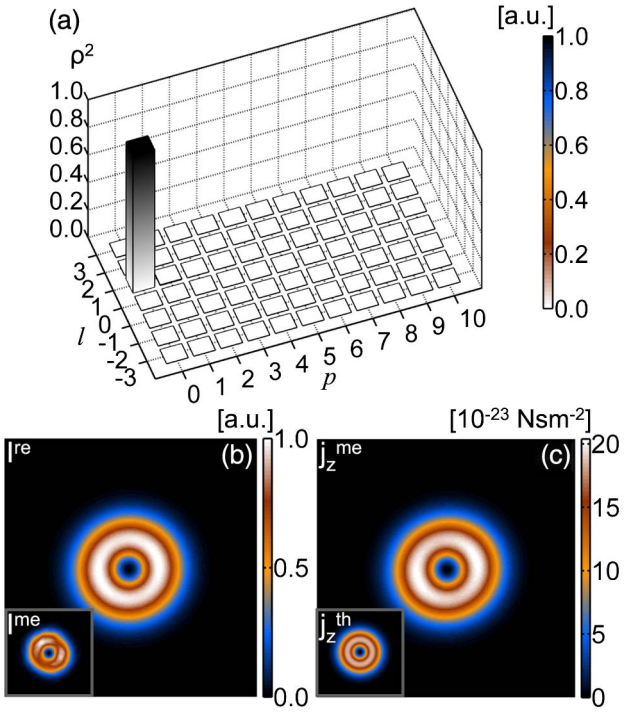

Fig. 4. Modal decomposition of an LG beam, $u_{0,1}$. (a) Mode spectrum. Reconstruction of (b) beam intensity and (c) OAM density. The insets depict the measured beam intensity and theoretical OAM density, respectively. The depicted section is 2.4 mm × 2.4 mm.

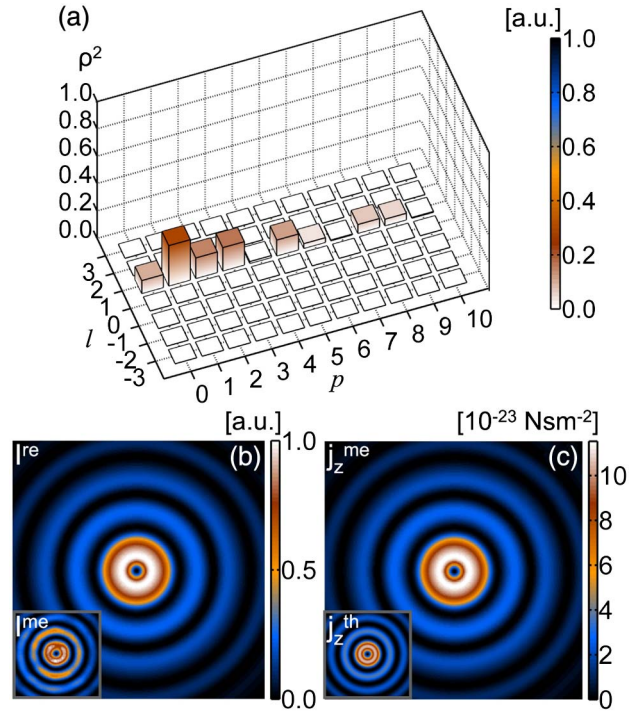

Fig. 5. Modal decomposition of a Bessel beam, $J_1 \exp(i\phi)$. (a) Mode spectrum. Reconstruction of (b) beam intensity and (c) OAM density. The insets depict the measured beam intensity and theoretical OAM density, respectively. The depicted section is 2.4 mm × 2.4 mm.

into LG modes of the same intrinsic scale, $w = 0.3$ mm, and of indices $l = -3 \ldots 3$ and $p = 0 \ldots 10$. In Fig. 4(a) the modal spectrum reveals the content of one single mode, which is the $u_{0,1}$ mode, as expected. In addition to the power spectrum the relative phases of all modes were measured and the beam intensity was reconstructed using Eq. (3). Figure 4(b) shows the typical ring-shaped intensity, which is in good agreement with the directly measured beam intensity (CCD_2, inset). The measured OAM density in units of Nsm^{-2} is depicted in Fig. 4(c) in addition to the theoretical OAM density, revealing good agreement. The fact that the OAM density and beam intensity look identical can be understood from Eq. (8), which elucidates that the OAM density is directly proportional to the intensity for beams of a single l value. For the same reason, the OAM density is all positive and does not change sign within the whole measurement area, caused by the positive sign of l [Eq. (8)]. By choosing the same intrinsic scale of the generated beam and decomposition modes, the mode set is perfectly adapted, yielding a single response in the mode spectrum. This is completely different when a Bessel beam of the same azimuthal index, $l = 1$ (intrinsic radius $w_b = 0.2$ mm), is decomposed into LG modes ($w = 0.3$ mm), which is shown in Fig. 5. As outlined in Section 3, when decomposing a Bessel beam into LG modes, only those modes of equal azimuthal index appear, which is confirmed by the modal power spectrum in Fig. 5(a). In contrast to the previous example in Fig. 4, however, those modes are dispersed over a range of radial indices, p. The number of relevant modes found in the experiment is in good agreement with the prediction of Fig. 1. Note that the chosen range of p values ($p = 0 \ldots 10$) is slightly larger than the actual required number of modes given in Fig. 1, at $w = 0.3$ mm. This was done to prove that the chosen range of mode indices is sufficient for reconstruction, i.e., some of the modes can be neglected. Again, from modal amplitudes and phases, the beam intensity [Fig. 5(b)] and OAM density [Fig. 5(c)] were reconstructed, matching the directly measured intensity and the theoretical OAM density. As in the previous case, the intensity distribution resembles the OAM density, and the OAM density is entirely positive, although the beam consists of a sum of modes. This is because only one azimuthal index, l, is involved in the superposition, where the OAM density is directly proportional to the beam intensity and l, according to Eq. (8).

To demonstrate that the decomposition of Bessel beams in LG modes is a versatile approach, we generated two different superpositions of Bessel beams yielding more complicated OAM density distributions. First, we considered an equally weighted superposition of two Bessel beams of opposite handiness in phase $J_3(q_1 r) \exp(3i\phi) + J_{-3}(q_2 r) \exp(-3i\phi)$ ($w_b = 0.2$ mm), and decomposed it into LG modes, with $w = 0.5$ mm as depicted in Fig. 6. In the mode spectrum now two traces of radial modes can be seen at $l = 3$ and $l = -3$. The corresponding intensity

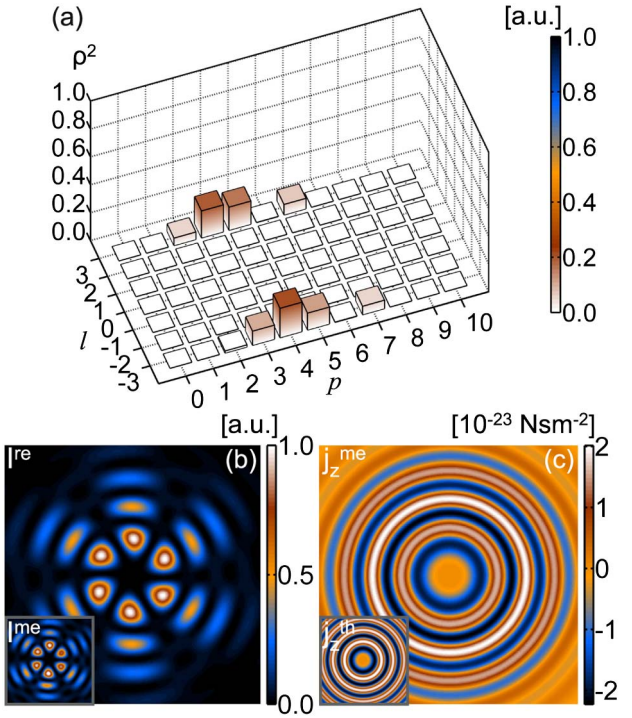

Fig. 6. Modal decomposition of a symmetric superposition of Bessel beams, $J_3(q_1 r)\exp(3i\phi) + J_{-3}(q_2 r)\exp(-3i\phi)$. (a) Mode spectrum. Reconstruction of (b) beam intensity and (c) OAM density. The insets depict the measured beam intensity and theoretical OAM density, respectively. The depicted section is 2.4 mm × 2.4 mm.

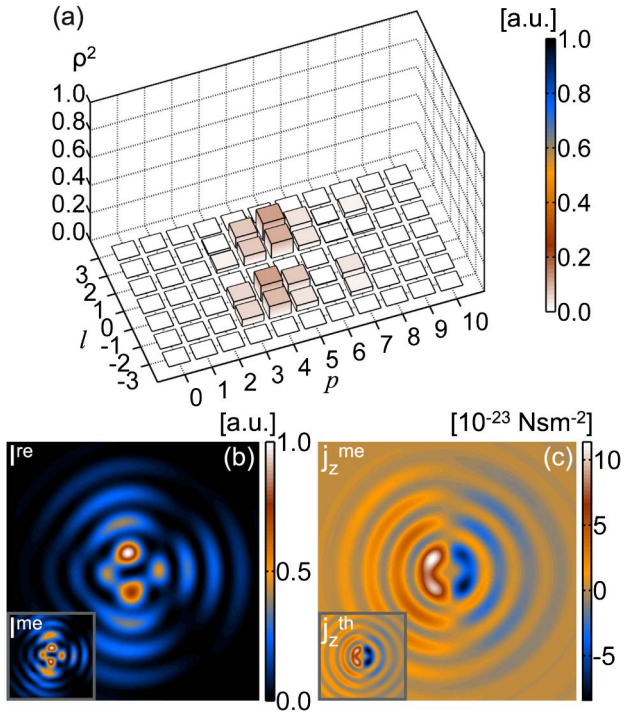

Fig. 7. Modal decomposition of a nonsymmetric superposition of Bessel beams, $J_2(q_1 r)\exp(2i\phi) + J_1(q_2 r)\exp(i\phi) + J_{-1}(q_3 r)\exp(-i\phi) + J_{-2}(q_4 r)\exp(-2i\phi)$. (a) Mode spectrum. Reconstruction of (b) beam intensity and (c) OAM density. The insets depict the measured beam intensity and theoretical OAM density, respectively. The depicted section is 2.4 mm × 2.4 mm.

pattern consists of six petals that are formed by the coherent Bessel superposition [cf. Fig. 6(b)]. If the scale of both Bessel beams were chosen to be exactly the same, the OAM density would vanish at every point of the field. For this reason, we detuned the scale of both beams slightly to yield an OAM density that oscillates between positive and negative parts, as shown in Fig. 6(c). As a result, the OAM density and beam intensity differ from each other, since more than one azimuthal index l is involved in the superposition. Although the correlation of the measured and theoretical OAM density is very good, it is noticeable that the OAM reconstruction becomes faint toward the rim. This is a direct result of both the limited extension of the LG modes compared to the Bessel beam and the restriction to a finite number of modes. Reconstruction within a larger region would, consequently, require the use of more modes for decomposition.

A superposition of four Bessel beams, $J_2(q_1 r)\exp(2i\phi) + J_1(q_2 r)\exp(i\phi) + J_{-1}(q_3 r)\exp(-i\phi) + J_{-2}(q_4 r)\exp(-2i\phi)$ is shown in Fig. 7. Again, each single Bessel beam was slightly detuned in scale, around $w_b = 0.2$ mm, and characterized by decomposition into LG modes of intrinsic scale, $w = 0.5$ mm. This time, four traces of radial modes appear in the spectrum [Fig. 7(a)]. As a result of the superposition the intensity becomes asymmetric [Fig. 7(b)], whereas the OAM density distribution is split into two halves with oscillations with opposed signs [Fig. 7(c)]. Again, beam intensity and OAM density are dissimilar due to the inclusion of several azimuthal modes of different l. Both beam intensity and OAM density are in very good agreement with the directly measured intensity and the theoretical OAM density distribution, revealing the high accuracy achieved with the modal decomposition.

8. Comparison to Azimuthal Decomposition

Besides the correlation-based modal decomposition, the only other technique for OAM density reconstruction is the azimuthal decomposition [16]. It is hence worthwhile to compare the achieved results to the example of Bessel beams.

The azimuthal decomposition technique is based on the same principle as the modal decomposition technique by means of an all-optical inner product measurement performed by correlation or matched filters (cf. Section 4). The only difference between the two types of decomposition lies in the definition of the matched filter. Unlike the modal decomposition, which requires the matched filter to be assigned as a 2D orthonormal basis (e.g., LG basis functions), the matched filter for the azimuthal decomposition is described in terms of 1D azimuthal phase variations, $\exp(il\phi)$. In analogy to Eq. (3), the optical field, U, can hence be described as [43]

$$U(r,\phi) = \sum_l c_l(r)\,\exp(il\phi), \tag{9}$$

where $c_l(r) = \varrho_l(r)\,\exp[i\varphi_l(r)]$. Note that a radial index is not necessary here. Instead, the radial dependence is moved into the expansion coefficient $c_l(r)$, which is in contrast to Eq. (3), where $c_{p,l}$ is a constant for given indices, p and l. The outstanding benefit of this azimuthal decomposition is the independence of the basis functions $\exp(il\phi)$ from the spatial scale, which was discussed in Section 3 as the crucial parameter when using a correlation filter, since it influences the signal-to-noise ratio and the number of modes and hence the required measurement time [49]. The advantage of this scale invariance is accompanied by the need for restoring the radial dependence of the beam by other means. Accordingly, the azimuthal matched filter function $\exp(il\phi)$ must be bounded by a ring-slit,

$$T_l(r,\phi) = \begin{cases} \exp(il\phi) & R - \frac{\Delta R}{2} < r < R + \frac{\Delta R}{2} \\ 0 & \text{otherwise} \end{cases}, \tag{10}$$

whose width ΔR represents the spatial resolution with which the OAM density can finally be reconstructed [43]. With these azimuthal matched filters, the amplitude functions $\rho_l(r)$ associated with each azimuthal mode $\exp(il\phi)$ at a set radial coordinate r can be extracted [55]. Similarly, their relative phase functions $\varphi_l(r)$ are inferred from the interference of the azimuthal mode $\exp(il\phi)$ with a reference wave, which may be implemented as an external source or, for convenience, the first mode in the series, $l = 0$, at a specific value of r [43]. The quantitative OAM density of a field is then determined in complete analogy to the derivations in Section 5 by either reconstructing the field or by calculating it directly from the azimuthal decomposition [16], similar to Eq. (7).

Using the azimuthal decomposition, the OAM density of the symmetric superposition, $J_3(q_1 r)\,\exp(3i\phi) + J_{-3}(q_2 r)\,\exp(-3i\phi)$, which was shown already in Fig. 6, and a nonsymmetric superposition of Bessel beams, $J_{-3}(q_1 r)\,\exp(-3i\phi) + J_2(q_2 r)\,\exp(2i\phi) + J_1(q_3 r)\,\exp(i\phi)$, was measured. In comparing the reconstructed intensity and OAM density for the symmetric (Fig. 8) and nonsymmetric (Fig. 9) superposition for each of the two decomposition techniques, we can see that there is good agreement between both methods, as well as to the directly measured intensity, and the theoretical OAM density, respectively, which are depicted as insets. However, it can be seen that the azimuthal decomposition is limited in radial resolution by the ring-slit width, which becomes particularly obvious when the intensity or OAM density distribution is nonsymmetric.

For both techniques, a reasonable number of modes is necessary for proper reconstruction of the field and the OAM density. Since both the LG and azimuthal modes constitute an infinite series,

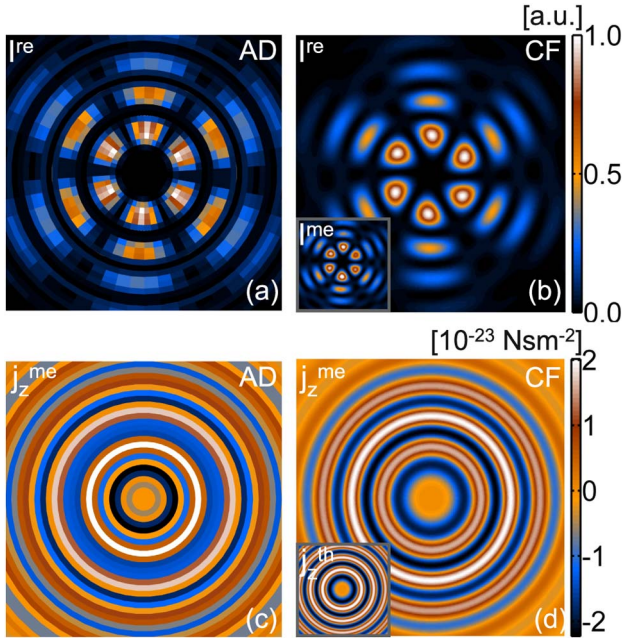

Fig. 8. Decomposition of a symmetric superposition of two Bessel beams, $J_3(q_1 r)\,\exp(3i\phi) + J_{-3}(q_2 r)\,\exp(-3i\phi)$. (a), (b) Reconstructed beam intensity from azimuthal decomposition (AD) and from modal decomposition using a correlation filter (CF); (c), (d) reconstructed OAM density from azimuthal decomposition (AD) and from using a correlation filter (CF). The insets depict the directly measured beam intensity and theoretical OAM density. The depicted section is 2.4 mm × 2.4 mm.

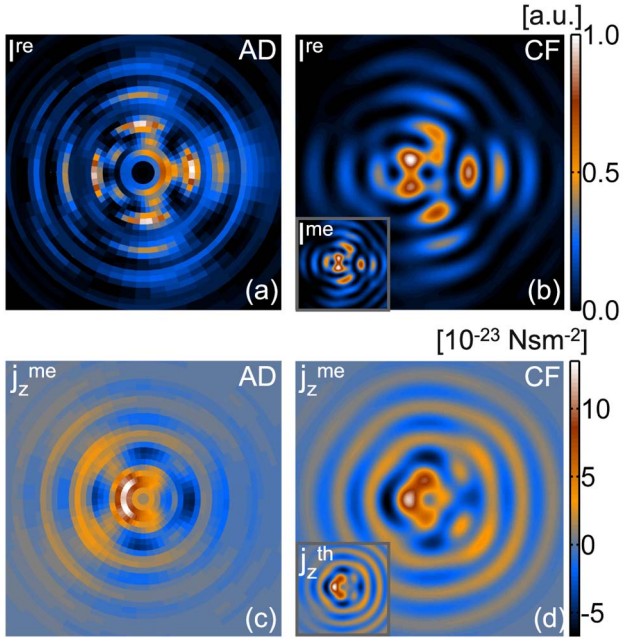

Fig. 9. Decomposition of a nonsymmetric superposition of three Bessel beams, $J_{-3}(q_1 r)\,\exp(-3i\phi) + J_2(q_2 r)\,\exp(2i\phi) + J_1(q_3 r)\,\exp(i\phi)$. (a), (b) Reconstructed beam intensity from azimuthal decomposition (AD) and from modal decomposition using a correlation filter (CF); (c), (d) reconstructed OAM density from azimuthal decomposition (AD) and from using a correlation filter (CF). The insets depict the directly measured beam intensity and theoretical OAM density. The depicted section is 2.4 mm × 2.4 mm.

selecting these modes when executing either decomposition might pose a challenge if one has no prior knowledge of the field. In this case, both techniques can be approached in an iterative (although time-consuming) manner as outlined in Section 3. An estimation of the azimuthal modes present in the field can again be obtained by displaying the respective phase patterns, $\exp(il\phi)$, (without amplitude modulation) and scanning through different values of l. As implied by Eq. (9), for the azimuthal decomposition technique, a range of radial coordinates, r, will need to be sampled when reconstructing a field (be it either Bessel or LG), but the choice of the ring-slit width and the number of ring-slits sampled will dictate the resolution and quality of the reconstructed field. In comparison, the modal decomposition (when implementing the LG basis as the matched filter) will require the same range of azimuthal indices, l, but also require a range of radial indices, p, e.g., in order to reconstruct the concentric ring structure present in Bessel beams. So, depending on the number of radial indices required for modal decomposition, either one of the techniques can be faster. In the presented examples, however, the beams were sampled with about 30 ring-slits regarding the azimuthal decomposition, whereas 10 radial LG modes were used with the correlation filter. For each radial mode, and for each ring-slit, respectively, the phase delay was measured in addition to the amplitude. Accordingly, the number of correlation measurements for the investigated beams was reduced by a factor of three when using the correlation filter-based modal decomposition, yielding a measurement duration of about 1 min. For both techniques, the measurement process could be sped up by angular multiplexing the single transmission functions, as detailed in [53]. However, for simplicity, all phase patterns were displayed, subsequently, on the corresponding SLM (SLM_2, cf. Section 6 and Fig. 3).

In terms of spatial resolution, the resolution of the SLM of 8 μm is finally limiting for both techniques (cf. Section 6). In the case of the correlation filter, the OAM density was hence reconstructed with 300 pixels × 300 pixels, whereas, for the azimuthal decomposition, the number of sampled ring-slits is the critical parameter. In the experiments the radial resolution was set to about 80 μm. In principle, the radial resolution could be improved by correlating the incident field with thinner ring-slits. However, this will simultaneously yield a significant drop in transmitted power and hence complicate detection. In comparison, the transmitting area is much larger when displaying an LG mode, such that the signal-to-noise ratio is, generally, larger using the correlation filter.

Even though the modal decomposition is advantageous in terms of spatial resolution and signal-to-noise ratio, this technique is scale-dependent: if the scale parameter, w, of the LG modes is incorrectly selected, this will translate into an unnecessary large number of modes and hence into a worse signal-to-noise ratio and longer measurement durations, rendering its benefits void. To circumvent this limitation, in addition to choosing a suitable mode basis, its spatial scale should be determined by measuring the beam propagation ratio and beam diameter, which can be done digitally using the same setup as shown in Fig. 3 [49] (cf. Section 3). The azimuthal decomposition on the other side overcomes this issue of scale dependence, but at the cost of spatial resolution, signal-to-noise ratio, and computation time; more ring-slits (i.e., matched filters) are required for sensible reconstruction.

9. Conclusion

To summarize, we demonstrated the quantitative OAM density measurement on pure and superimposed Bessel beams by projection into Laguerre–Gaussian (LG) modes. The projection was realized by modal decomposition with correlation filters. In contrast to previous studies, it was shown that such decomposition is not limited to superpositions of LG beams but can equally be used to characterize arbitrary beam shapes, such as superpositions of Bessel beams. By choosing the spatial scale of the LG basis correctly, the number of radial modes necessary to reconstruct the OAM density can be small; e.g., about ten radial modes were required in the presented experiments. In comparison to the previously published azimuthal decomposition, the decomposition into LG modes stands out by its high spatial resolution, reduced measurement time, and improved signal-to-noise ratio. In contrast, the main benefit of the azimuthal decomposition is its independence of the spatial scale, which must be determined separately by an additional measurement concerning the modal decomposition technique. Given the spatial scale, the correlation filter-based modal decomposition enables a fast and robust measurement of the OAM density even in the case of highly multimode fields, whereas reconstruction fidelities of up to 95% were reached.

References

1. L. Allen, M. W. Beijersbergen, R. J. C. Spreeuw, and J. P. Woerdman, "Orbital angular momentum of light and the transformation of Laguerre-Gaussian laser modes," Phys. Rev. A **45**, 8185–8189 (1992).
2. M. Padgett, J. Courtial, and L. Allen, "Light's orbital angular momentum," Phys. Today **57**(5), 35–40 (2004).
3. S. Franke-Arnold, L. Allen, and M. Padgett, "Advances in optical angular momentum," Laser Photon. Rev. **2**, 299–313 (2008).
4. A. M. Yao and M. J. Padgett, "Orbital angular momentum: origins, behavior and applications," Adv. Opt. Photon. **3**, 161–204 (2011).
5. M. E. J. Friese, J. Enger, H. Rubinsztein-Dunlop, and N. R. Heckenberg, "Optical angular-momentum transfer to trapped absorbing particles," Phys. Rev. A **54**, 1593–1596 (1996).
6. V. Garcés-Chávez, D. McGloin, M. J. Padgett, W. Dultz, H. Schmitzer, and K. Dholakia, "Observation of the transfer of the local angular momentum density of a multiringed light beam to an optically trapped particle," Phys. Rev. Lett. **91**, 093602 (2003).
7. Y. Zhao, D. Shapiro, D. Mcgloin, D. T. Chiu, and S. Marchesini, "Direct observation of the transfer of orbital angular momentum to metal particles from a focused circularly polarized Gaussian beam," Opt. Express **17**, 23316–23322 (2009).

8. K. Dholakia and T. Cizmar, "Shaping the future of manipulation," Nat. Photonics **5**, 335–342 (2011).
9. M. Padgett and R. Bowman, "Tweezers with a twist," Nat. Photonics **5**, 343–348 (2011).
10. R. Fickler, R. Lapkiewicz, W. N. Plick, M. Krenn, C. Schaeff, S. Ramelow, and A. Zeilinger, "Quantum entanglement of high angular momenta," Science **338**, 640–643 (2012).
11. G. Gibson, J. Courtial, M. Padgett, M. Vasnetsov, V. Pas'ko, S. Barnett, and S. Franke-Arnold, "Free-space information transfer using light beams carrying orbital angular momentum," Opt. Express **12**, 5448–5456 (2004).
12. J. Wang, J.-Y. Yang, I. M. Fazal, N. Ahmed, Y. Yan, H. Huang, Y. Ren, Y. Yue, S. Dolinar, M. Tur, and A. E. Willner, "Terabit free-space data transmission employing orbital angular momentum multiplexing," Nat. Photonics **6**, 488–496 (2012).
13. N. Bozinovic, Y. Yue, Y. Ren, M. Tur, P. Kristensen, H. Huang, A. E. Willner, and S. Ramachandran, "Terabit-scale orbital angular momentum mode division multiplexing in fibers," Science **340**, 1545–1548 (2013).
14. L. Allen and M. J. Padgett, "The Poynting vector in Laguerre-Gaussian beams and the interpretation of their angular momentum density," Opt. Commun. **184**, 67–71 (2000).
15. N. Bozinovic, S. Golowich, P. Kristensen, and S. Ramachandran, "Control of orbital angular momentum of light with optical fibers," Opt. Lett. **37**, 2451–2453 (2012).
16. A. Dudley, I. A. Litvin, and A. Forbes, "Quantitative measurement of the orbital angular momentum density of light," Appl. Opt. **51**, 823–833 (2012).
17. I. A. Litvin, M. G. McLaren, and A. Forbes, "A conical wave approach to calculating Bessel-Gauss beam reconstruction after complex obstacles," Opt. Commun. **282**, 1078–1082 (2009).
18. M. McLaren, T. Mhlanga, M. J. Padgett, F. S. Roux, and A. Forbes, "Self-healing of quantum entanglement after an obstruction," Nat. Commun. **5**, 1–8 (2014).
19. K. Volke-Sepulveda, V. Garcés-Chávez, S. Chávez-Cerda, J. Arlt, and K. Dholakia, "Orbital angular momentum of a high-order Bessel light beam," J. Opt. B **4**, S82–S89 (2002).
20. W. M. Lee, X.-C. Yuan, and W. C. Cheong, "Optical vortex beam shaping by use of highly efficient irregular spiral phase plates for optical micromanipulation," Opt. Lett. **29**, 1796–1798 (2004).
21. M. Mirhosseini, O. S. Magaña-Loaiza, C. Chen, B. Rodenburg, M. Malik, and R. W. Boyd, "Rapid generation of light beams carrying orbital angular momentum," Opt. Express **21**, 30196–30203 (2013).
22. M. Zurch, C. Kern, P. Hansinger, A. Dreischuh, and C. Spielmann, "Strong-field physics with singular light beams," Nat. Phys. **8**, 743–746 (2012).
23. B. J. McMorran, A. Agrawal, I. M. Anderson, A. A. Herzing, H. J. Lezec, J. J. McClelland, and J. Unguris, "Electron vortex beams with high quanta of orbital angular momentum," Science **331**, 192–195 (2011).
24. J. Courtial, K. Dholakia, L. Allen, and M. Padgett, "Gaussian beams with very high orbital angular momentum," Opt. Commun. **144**, 210–213 (1997).
25. S.-C. Chu, T. Ohtomo, and K. Otsuka, "Generation of doughnutlike vortex beam with tunable orbital angular momentum from lasers with controlled Hermite-Gaussian modes," Appl. Opt. **47**, 2583–2591 (2008).
26. T. Yusufu, Y. Tokizane, M. Yamada, K. Miyamoto, and T. Omatsu, "Tunable 2-μm optical vortex parametric oscillator," Opt. Express **20**, 23666–23675 (2012).
27. M. Koyama, T. Hirose, M. Okida, K. Miyamoto, and T. Omatsu, "Power scaling of a picosecond vortex laser based on a stressed Yb-doped fiber amplifier," Opt. Express **19**, 994–999 (2011).
28. A. Mair, A. Vaziri, G. Weihs, and A. Zeilinger, "Entanglement of the orbital angular momentum states of photons," Nature **412**, 313–316 (2001).
29. C. Smith and R. McDuff, "Charge and position detection of phase singularities using holograms," Opt. Commun. **114**, 37–44 (1995).
30. P. Genevet, J. Lin, M. A. Kats, and F. Capasso, "Holographic detection of the orbital angular momentum of light with plasmonic photodiodes," Nat. Commun. **3**, 1278 (2012).
31. J. M. Hickmann, E. J. S. Fonseca, W. C. Soares, and S. Chávez-Cerda, "Unveiling a truncated optical lattice associated with a triangular aperture using light's orbital angular momentum," Phys. Rev. Lett. **105**, 053904 (2010).
32. J. Courtial, K. Dholakia, D. A. Robertson, L. Allen, and M. J. Padgett, "Measurement of the rotational frequency shift imparted to a rotating light beam possessing orbital angular momentum," Phys. Rev. Lett. **80**, 3217–3219 (1998).
33. M. V. Vasnetsov, J. P. Torres, D. V. Petrov, and L. Torner, "Observation of the orbital angular momentum spectrum of a light beam," Opt. Lett. **28**, 2285–2287 (2003).
34. J. Leach, M. J. Padgett, S. M. Barnett, S. Franke-Arnold, and J. Courtial, "Measuring the orbital angular momentum of a single photon," Phys. Rev. Lett. **88**, 257901 (2002).
35. M. P. J. Lavery, A. Dudley, A. Forbes, J. Courtial, and M. J. Padgett, "Robust interferometer for the routing of light beams carrying orbital angular momentum," New J. Phys. **13**, 093014 (2011).
36. A. Belmonte and J. P. Torres, "Digital coherent receiver for orbital angular momentum demultiplexing," Opt. Lett. **38**, 241–243 (2013).
37. V. P. Aksenov, I. V. Izmailov, F. Y. Kanev, and B. N. Poizner, "Optical vortex detector as a basis for a data transfer system: operational principle, model, and simulation of the influence of turbulence and noise," Opt. Commun. **285**, 905–928 (2012).
38. G. C. G. Berkhout, M. P. J. Lavery, J. Courtial, M. W. Beijersbergen, and M. J. Padgett, "Efficient sorting of orbital angular momentum states of light," Phys. Rev. Lett. **105**, 153601 (2010).
39. M. P. J. Lavery, G. C. G. Berkhout, J. Courtial, and M. J. Padgett, "Measurement of the light orbital angular momentum spectrum using an optical geometric transformation," J. Opt. **13**, 064006 (2011).
40. M. P. J. Lavery, D. J. Robertson, A. Sponselli, J. Courtial, N. K. Steinhoff, G. A. Tyler, A. Wilner, and M. J. Padgett, "Efficient measurement of an optical orbital-angular-momentum spectrum comprising more than 50 states," New J. Phys. **15**, 013024 (2013).
41. A. Dudley, T. Mhlanga, M. Lavery, A. McDonald, F. S. Roux, M. Padgett, and A. Forbes, "Efficient sorting of Bessel beams," Opt. Express **21**, 165–171 (2013).
42. M. P. J. Lavery, D. J. Robertson, G. C. G. Berkhout, G. D. Love, M. J. Padgett, and J. Courtial, "Refractive elements for the measurement of the orbital angular momentum of a single photon," Opt. Express **20**, 2110–2115 (2012).
43. I. A. Litvin, A. Dudley, F. S. Roux, and A. Forbes, "Azimuthal decomposition with digital holograms," Opt. Express **20**, 10996–11004 (2012).
44. C. Schulze, A. Dudley, D. Flamm, M. Duparré, and A. Forbes, "Measurement of the orbital angular momentum density of light by modal decomposition," New J. Phys. **15**, 073025 (2013).
45. J. C. Gutiérrez-Vega, M. D. Iturbe-Castillo, and S. Chávez-Cerda, "Alternative formulation for invariant optical fields: Mathieu beams," Opt. Lett. **25**, 1493–1495 (2000).
46. M. A. Bandres and J. Gutiérrez-Vega, "Ince-Gaussian beams," Opt. Lett. **29**, 144–146 (2004).
47. J. W. Goodman, *Introduction to Fourier Optics*, 3rd ed. (Roberts & Company, 2005).
48. J. L. Rodgers and W. A. Nicewander, "Thirteen ways to look at the correlation coefficient," Am. Stat. **42**, 59–66 (1988).
49. C. Schulze, S. Ngcobo, M. Duparré, and A. Forbes, "Modal decomposition without a priori scale information," Opt. Express **20**, 27866–27873 (2012).
50. A. E. Siegman, "New developments in laser resonators," Proc. SPIE **1224**, 2–14 (1990).
51. M. A. Golub, A. M. Prokhorov, I. N. Sisakian, and V. A. Soifer, "Synthesis of spatial filters for investigation of the transverse mode composition of coherent radiation," Sov. J. Quantum Electron. **9**, 1866–1868 (1982).

52. H. Bartelt, A. Lohmann, W. Freude, and G. Grau, "Mode analysis of optical fibres using computer-generated matched filters," Electron. Lett. **19**, 247–249 (1983).
53. T. Kaiser, D. Flamm, S. Schröter, and M. Duparré, "Complete modal decomposition for optical fibers using CGH-based correlation filters," Opt. Express **17**, 9347–9356 (2009).
54. V. Arrizón, U. Ruiz, R. Carrada, and L. A. González, "Pixelated phase computer holograms for the accurate encoding of scalar complex fields," J. Opt. Soc. Am. A **24**, 3500–3507 (2007).
55. I. A. Litvin, A. Dudley, and A. Forbes, "Poynting vector and orbital angular momentum density of superpositions of Bessel beams," Opt. Express **19**, 16760–16771 (2011).